

An optical coherence microscope for 3-dimensional imaging in developmental biology

Barbara M. Hoeling[†], Andrew D. Fernandez[§], Richard C. Haskell[†], Eric Huang[†],
Whittier R. Myers[†], Daniel C. Petersen[†], Sharon E. Ungersma[†], Ruye Wang[§],
and Mary E. Williams^{*}

Biology^{*}, Engineering[§], and Physics[†] Departments
Harvey Mudd College, 301 East Twelfth Street, Claremont, CA 91711
Richard_Haskell@hmc.edu

Scott E. Fraser

Biological Imaging Center, California Institute of Technology, 1200 East California Boulevard, Pasadena, CA 91125

Abstract: An optical coherence microscope (OCM) has been designed and constructed to acquire 3-dimensional images of highly scattering biological tissue. Volume-rendering software is used to enhance 3-D visualization of the data sets. Lateral resolution of the OCM is 5 μm (FWHM), and the depth resolution is 10 μm (FWHM) in tissue. The design trade-offs for a 3-D OCM are discussed, and the fundamental photon noise limitation is measured and compared with theory. A rotating 3-D image of a frog embryo is presented to illustrate the capabilities of the instrument.

©1999 Optical Society of America

OCIS codes: (170.4500) Optical coherence tomography; (170.6900) Three-dimensional microscopy; (110.6880) Three-dimensional image acquisition; (120.3180) Interferometry

References and links

1. J.A. Izatt, M.D. Kulkarni, H.-W. Wang, K. Kobayashi, and M.V. Sivak, Jr., "Optical coherence tomography and microscopy in gastrointestinal tissues," *IEEE J. Sel. Topics Quant. Electron.* **2**, 1017-1028 (1996).
2. A.M. Rollins, M.D. Kulkarni, S. Yazdanfar, R. Ung-arnyawee, and J.A. Izatt, "In vivo video rate optical coherence tomography," *Optics Express* **3**, 219-229 (1998).
3. S. Yazdanfar, M.D. Kulkarni, and J.A. Izatt, "High resolution imaging of *in vivo* cardiac dynamics using color Doppler optical coherence tomography," *Optics Express* **1**, 424-431 (1997).
4. S.A. Boppart, M.E. Brezinski, B.E. Bouma, G.J. Tearney, and J.G. Fujimoto, "Investigation of developing embryonic morphology using optical coherence tomography," *Dev. Biol.* **177**, 54-63 (1996).
5. S.A. Boppart, B.E. Bouma, M.E. Brezinski, G.J. Tearney, and J.G. Fujimoto, "Imaging developing neural morphology using optical coherence tomography," *J. Neurosci. Methods* **70**, 65-72 (1996).
6. S.A. Boppart, G.J. Tearney, B.E. Bouma, J.F. Southern, M.E. Brezinski, and J.G. Fujimoto, "Noninvasive assessment of the developing *Xenopus* cardiovascular system using optical coherence tomography," *Proc. Natl. Acad. Sci.* **94**, 4256-4261 (1997).
7. S.A. Boppart, B.E. Bouma, C. Pitris, J.F. Southern, M.E. Brezinski, and J.G. Fujimoto, "In vivo cellular optical coherence tomography imaging," *Nature Medicine* **4**, 861-865 (1998).
8. S.A. Boppart, M.E. Brezinski, C. Pitris, J.G. Fujimoto, "Optical coherence tomography for neurosurgical imaging of human intracortical melanoma," *Neurosurgery* **43**, 834-841 (1998).
9. J.M. Herrmann, M.E. Brezinski, B.E. Bouma, S.A. Boppart, C. Pitris, J.F. Southern, and J.G. Fujimoto, "Two- and three-dimensional high-resolution imaging of the human oviduct with optical coherence tomography," *Fertility and Sterility* **70**, 155-158 (1998).
10. S.A. Boppart, B.E. Bouma, C. Pitris, G.J. Tearney, J.F. Southern, M.E. Brezinski, and J.G. Fujimoto, "Intraoperative assessment of microsurgery with three-dimensional optical coherence tomography," *Radiology* **208**, 81-86 (1998).
11. A.F. Fercher, "Optical coherence tomography," *J. Biomed. Optics* **1**, 157-173 (1996).
12. B.R. Masters, "Early development of optical low-coherence reflectometry and some recent biomedical applications," *J. Biomed. Optics* **4**, 236-247 (1999).
13. S.R. Chinn and E.A. Swanson, "Blindness limitations in optical coherence domain reflectometry," *Electronics Letters* **29**, 2025-2027 (1993)

14. G.J. Tearney, B.E. Bouma, S.A. Boppart, B. Golubovic, E.A. Swanson, and J.G. Fujimoto, "Rapid acquisition of *in vivo* biological images by use of optical coherence tomography," *Optics Letters* **21**, 1408-1410 (1996).
 15. M.D. Duncan, M. Bashkansky, and J. Reintjes, "Subsurface defect detection in materials using optical coherence tomography," *Optics Express* **2**, 540-545 (1998).
 16. M. Imai, T. Yano, K. Motoi, and A. Odajima, "Piezoelectrically induced optical phase modulation of light in single-mode fibers," *J. Quantum Electronics* **28**, 1901-1908 (1992).
 17. W.V. Sorin and D.M. Baney, "A simple intensity noise reduction technique for optical low-coherence reflectometry," *IEEE Photonics Technology Letters* **4**, 1404-1406 (1992).
 18. B. Saleh, Equation 5.93 in *Photoelectron Statistics* (Springer-Verlag, New York 1978).
 19. A. Kaufman, "Trends in volume visualization and volume graphics" in *Scientific Visualization*, L. Rosenblum, ed. (Academic, San Diego, CA 1994).
-

1. Introduction

We have constructed an optical coherence microscope (OCM) to image critical events in the early development of plants and animals. The spatial relationships between cells and groups of cells are important in the development of tissue, so our OCM has been designed specifically to produce 3-dimensional images that can be rotated on a computer screen to achieve a 3-D perspective. Volume-rendering software enhances this 3-D visualization.

Izatt et al. [1] have compared optical coherence microscopy (OCM) with optical coherence tomography (OCT). Both are noninvasive techniques for imaging objects embedded up to 2 mm deep in highly scattering media, and both derive their depth resolution from the short coherence length of the light source employed. To achieve the higher resolution of OCM (3 to 10 μm versus 10 to 30 μm), special effort is usually made to keep the focused waist of the beam coincident with the equal path length position of the OCM interferometer, thus preserving the lateral resolution throughout the depth of the sample. At least two groups of researchers have explored the use of OCM in developmental biology [2-3, 4-7]. Image visualization has primarily consisted of examining successive 2-D optical slices, though occasional 3-D reconstructions have been made [6-10]. Even in the latter case, one dimension in the 3-D reconstruction covers a shorter distance or has poorer resolution. Our data acquisition and visualization procedures are designed to acquire data of comparable quality in all three dimensions and accentuate the 3-D structure of the tissue imaged.

The size of cells in developing plants and animals is typically 5 to 10 μm . In an attempt to resolve most cells, the beam in our OCM is focused to a waist of 5 μm (FWHM) which determines the lateral resolution (see Figure 1). To maintain this lateral resolution throughout the depth of the image, we perform 2-dimensional *en face* scans (in the plane normal to the beam axis) using a pair of galvoscaning mirrors. After each *en face* scan, the depth is incremented by moving the focusing lens while the position of the reference mirror is adjusted to keep the equal path length position of the OCM interferometer coincident with the beam waist. This procedure maintains a 5 μm lateral resolution throughout the image.

The choice of *en face* scanning leads necessarily to one instrumental complication. In most OCM instruments, output fringes are produced by the movement of the scanning reference mirror (see the reviews of OCT [11,12]). In our instrument, however, the reference mirror remains essentially stationary during each *en face* scan. We have found an inexpensive way to generate high frequency (125 KHz) output fringes by modulating the reference path length with small displacement oscillations (400 nm) of the reference mirror. A small, lightweight mirror is glued onto a piezo stack which is then driven at a resonance frequency of the mirror/piezo system. The high frequency of the reference mirror oscillation provides for fast image acquisition (~ 5 minutes), and the small modulation amplitude (~ 1 fringe) avoids degradation of the depth resolution.

Depth resolution in OCM is determined by the coherence length of the light source. We are using a superluminescent diode (SLD) with a center wavelength of 843 nm and a spectral

width of 21 nm (FWHM). The resulting depth resolution (FWHM) is 15 μm in air or approximately 10 μm in tissue ($n \sim 1.4$). Since the modulation of the reference path length is much smaller ($< 0.5 \mu\text{m}$), blurring of the image in the depth dimension is negligible.

The small phase modulation of the OCM interferometer does, however, lead to one additional instrumental complication. Temperature variations in the optical fibers of the OCM interferometer lead to slow phase drifts (~ 15 seconds) in the output, which in turn lead to slow drifts in the rms amplitude of the output fringes. We have followed the lead of previous researchers [1,13] in devising a measure of the fringe amplitude that is independent of this slow phase drift. The magnitude of the piezo-driving voltage is adjusted so that the displacement amplitude of the reference mirror oscillation reaches an optimal value of 0.42λ . At this value the sum of the powers in the output fringe signal at the first two harmonics of the piezo-driving frequency is insensitive to the slow phase drift. We use the square root of this sum of powers as a measure of fringe amplitude.

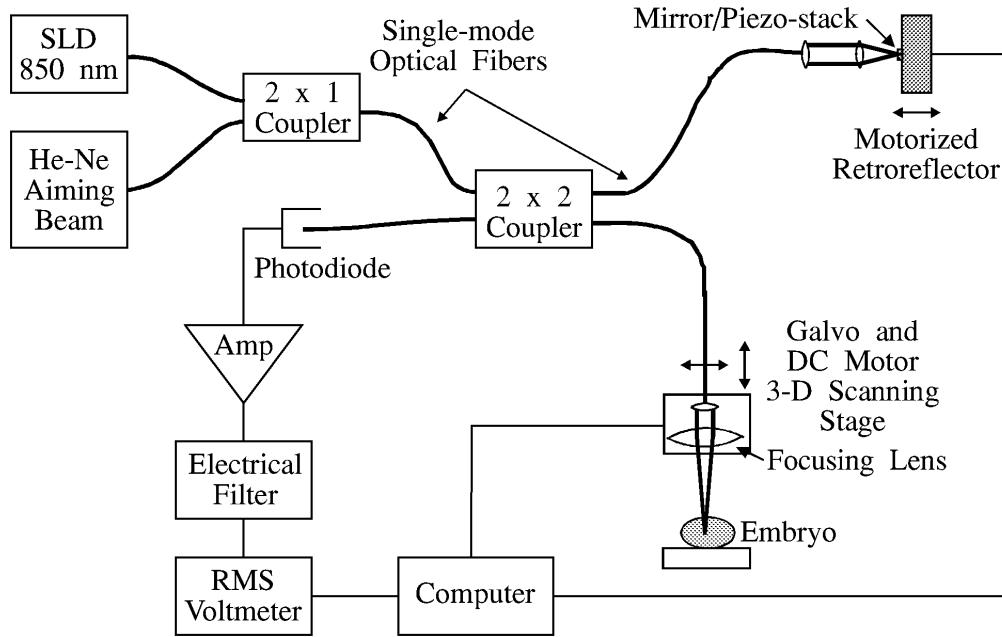


Fig. 1. Optical schematic of the optical coherence microscope.

In Section 2 of this paper we describe more completely the technique for phase modulation with the mirror/piezo stack system. Details of construction are included, and a quantitative analysis of the performance of the system is presented. In Section 3 we describe the fundamental photon noise limitation of the microscope. To maximize the signal-to-noise ratio, a neutral density filter is placed in the reference arm of the OCM interferometer to reduce the Bose-Einstein photon bunching of the SLD source. Finally, in Section 4 we describe our procedure for visualization of the 3-D images and include a rotating image of a developing frog embryo.

2. Fringe generation with a piezoelectric stack

Piezoelectric crystals have been used in a variety of forms for phase modulation in OCM. Our requirements, however, are unusual: we need a modulation frequency above 100 KHz for rapid image acquisition, a low amplitude of modulation to preserve depth resolution, and for convenience we would like to drive the piezo with a standard function generator. Izatt et

al. [1] attached an OCM reference mirror to a piezo stack and modulated with a low amplitude ($< 1 \mu\text{m}$) at 1.6 KHz, too low a frequency for our criteria. Other investigators have wrapped optical fiber around piezo materials, stretching and relaxing the fiber to modulate the path length. For example, Tearney et al. [14] achieved a fringe frequency of 5 MHz by modulating the reference path length by 3 mm, too large a modulation for our instrument. Duncan et al. [15] modulated the reference fiber length by a “few microns” and achieved a fringe frequency of 300 KHz. One problem associated with this technique is that the long lengths of fiber used (tens of meters) result in increased phase drift in the interferometer. Also, the longer fibers increase static polarization mismatch and dynamic birefringence modulation [14]. Alternatively, fibers coated with piezoelectric films have recently been used [16]. When a voltage is applied to the piezo jacket, the fiber is squeezed radially and thus increases in length. In this way, fast phase modulations can be achieved, but the modulation amplitude is typically small. In order to produce a change in optical path length of $1 \mu\text{m}$ at 100 KHz, a fiber coated over a length of 20 cm would require more than 100 volts of driving amplitude.

Our final solution for phase modulation is both inexpensive and convenient. A small plane mirror (1.5 mm x 1.5 mm x 0.1 mm, from Edmund Scientific Co., Barrington, NJ) is glued with cyanoacrylate (“super glue”) to a piezo stack (manufactured by NEC and available from Thorlabs Inc., Newton, NJ, type AE0203D04, 2.5 mm x 5 mm x 5 mm). The mirror/piezo stack system is epoxied (F120, from Thorlabs Inc., Newton, NJ) to an aluminum disk (25 mm diameter x 5 mm thick) which is then held in a mirror mount. The mirror mount is positioned so that the mirror lies in the focal plane of a lens, producing a cat’s eye retroreflector in the reference arm of the OCM. The piezo stack is driven at 125 KHz, a resonance frequency of the stack (not of the aluminum disk/mirror mount). A peak-to-peak driving voltage of 6.7 volts produces a displacement amplitude of 400 nm, or roughly one fringe at the OCM output. The stack does not heat up noticeably during operation and has proved to be remarkably stable over a year of nearly continuous operation.

While small modulations in the reference path length preserve good depth resolution in the OCM, a significant problem arises from the slow thermal drift of the optical path lengths in the interferometer reference and sample fibers. The interferometer output fringe signal takes on distinctly different shapes depending on the initial phase relation between the sample and

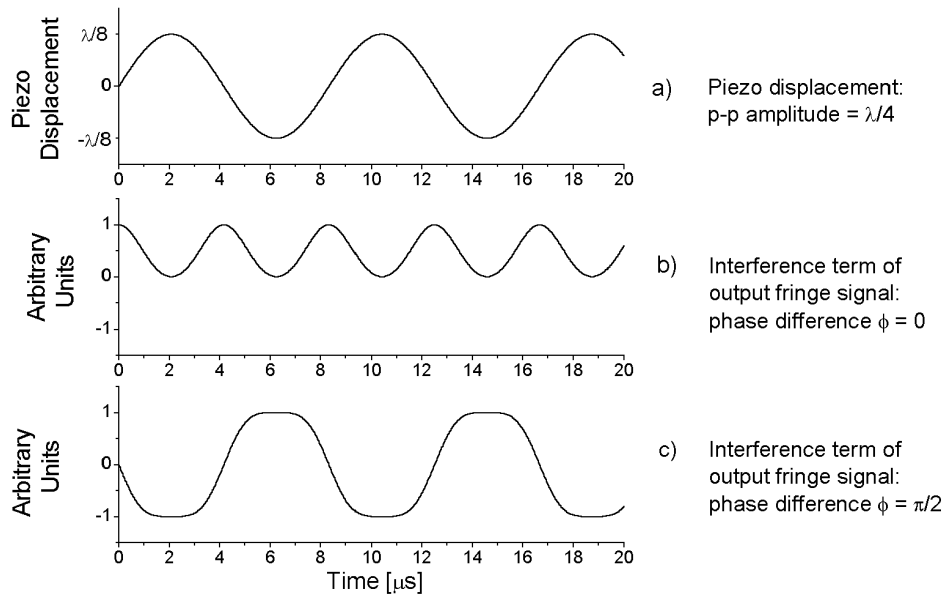


Fig. 2. Phase dependence of the output fringe signal.

reference beams. Figure 2 illustrates this point for a modulation of one-half fringe (piezo displacement of 0.25λ). Graph (a) in Figure 2 shows the piezo displacement $d_0 \sin \omega t$, where the peak-to-peak displacement $2d_0$ is taken to be 0.25λ . The interference term in the interferometer output intensity is given by

$$I_{out} = I_0 \cos(\alpha \sin \omega t + f) \quad (1)$$

where α is related to the piezo displacement amplitude by $\alpha = 4\pi d_0 / \lambda$, and I_0 is equal to $2\sqrt{I_{ref} I_{samp}}$, where I_{ref} and I_{samp} are the intensities returned from the reference and sample paths. Graph (b) in Figure 2 plots I_{out} for an initial phase difference between the sample and reference beams of $f = 0$. Graph (c) is a similar plot for $f = \pi/2$. The two signals are clearly different in shape and have different Fourier components, including different DC components. In Graph (b) the strongest AC component is the one at 2ω , the second harmonic of the piezo-driving frequency. In Graph (c) the signal's dominant Fourier component is the one at ω , the fundamental of the driving frequency. By inspection of the graphs, it also becomes clear that the rms values for the AC-coupled signals are different. (We must AC-couple the interferometer output in our OCM to eliminate the huge DC component I_{ref} .) Therefore random phase drifts between the sample and reference beams will lead to drifts in the rms value of the AC coupled interferometer output.

To circumvent this problem, we have followed the lead of previous investigators [1,13]. Calculating the Fourier components of the signal in equation (1), we can express the power P_1 in the fundamental frequency ω and the power P_2 in the second harmonic 2ω as:

$$P_1 = 2I_0^2 J_1^2(\alpha) \sin^2 f \quad (2)$$

$$P_2 = 2I_0^2 J_2^2(\alpha) \cos^2 f \quad (3)$$

where J_1 and J_2 are the first and second order Bessel functions. Thus the sum of the powers in the first two harmonics $P_1 + P_2$ is independent of f only for those piezo amplitudes for which $J_1^2(\alpha) = J_2^2(\alpha)$. The lowest value of α for which this occurs is $\alpha = 2.63$, leading to a piezo displacement $2d_0$ of 0.419λ . At this particular modulation amplitude, the sum $P_1 + P_2$

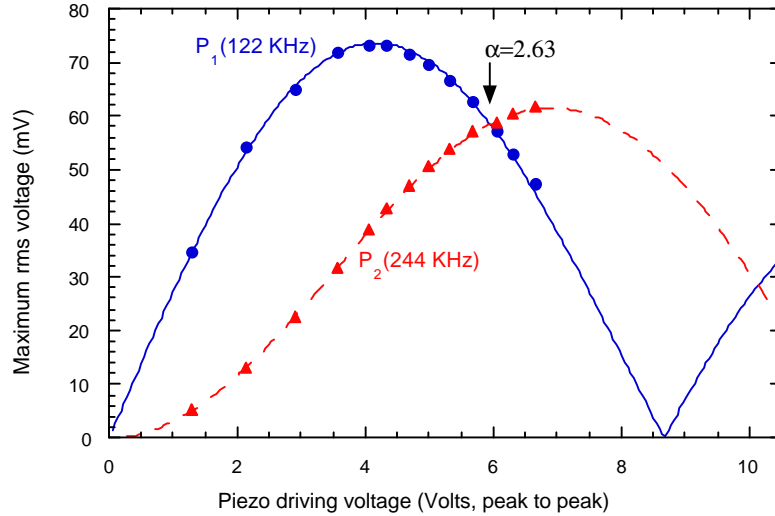


Fig. 3. Maximum powers in the output fringe signal at the first two harmonics of the piezo-driving voltage.

is independent of drifts in the pathlength difference between the two arms. We are using the square root of the sum as a measure of the AC-coupled interferometer output fringe amplitude.

Figure 3 shows the experimental values for the powers of the interferometer output signal in the first two harmonics as a function of the piezo driving voltage. For each setting of the driving voltage, the powers at 122 KHz and at 244 KHz were observed with a spectrum analyzer as they varied with the drifting phase, and their maximum values are plotted. The solid and dashed lines indicate the best fits to the equations $P_1 = k_1 J_1^2(r_1 x)$ and $P_2 = k_2 J_2^2(r_2 x)$, where k_1 , k_2 , r_1 , and r_2 are fitting parameters. As expected, the fitted values of k_1 and k_2 were the same to within 1%, and the values of $r_1 x$ and $r_2 x$ at a piezo voltage of $x = 5.95$ volts peak-to-peak were within 1% of 2.63. At this setting the sum of powers $P_1 + P_2$ was observed to be independent of phase drift.

3. Fundamental photon noise limitations

The speed of image acquisition and the signal-to-noise ratio (SNR) in OCM are ultimately limited by fundamental photon noise. Ordinarily one would expect this noise to be Poisson distributed, so that a stronger source provides a faster speed and greater SNR. This is only partially true. Like Sorin and Baney [17], we have found that the SNR in our OCM is improved by attenuating the power in the reference beam. Typical SLD sources operate with powers and coherence times that lead to photon noise dominated by Bose-Einstein photon bunching. Attenuating the reference beam power reduces the photon bunching and returns the instrument to the regime of Poisson noise. Of course an increase in the sample beam power will increase the SNR when imaging biological tissue, but the reference power must not be allowed to increase into the photon bunching regime. While our results confirm those of Sorin and Baney [17], we will use somewhat different language to describe this phenomenon theoretically.

The coherence time of our SLD is $t_{coh} = 60$ fs, and the sampling time of the photodetector electronics is $T = 1.25 \mu s$ ($T = 1/(2 \text{ BW})$ where the bandwidth $\text{BW} = 400$ KHz). The variance of the number of photons collected in a sampling time is [18]

$$\text{Var}(n) = \langle n \rangle + \frac{\langle n \rangle^2}{N} \quad (4)$$

where $N = T/t_{coh}$ is the (large) number of coherence times contained in the sampling time ($\sim 10^7$). The first term on the right-hand side of equation (4) is the Poisson contribution and the second represents the Bose-Einstein photon bunching. Actually the SLD emits two orthogonal, independent polarization states, so the variance becomes

$$\text{Var}(n) = 2 \left[\frac{\langle n \rangle}{2} + \frac{1}{N} \left(\frac{\langle n \rangle}{2} \right)^2 \right] = \langle n \rangle + \frac{1}{2} \frac{\langle n \rangle^2}{N} \quad (5)$$

The rms noise in the output of the photodetector electronics is primarily due to photon noise in the reference beam, but the contribution of amplifier noise must also be included:

$$V_{rms \text{ noise}} = g \sqrt{\left[(R \cdot NEP)^2 \cdot \text{BW} \right] + \left[2 \hbar e^2 \text{BW} \frac{P_{ref}}{E_n} \right] + \left[\left(\hbar e \frac{P_{ref}}{E_n} \right)^2 t_{coh} \text{BW} \right]} \quad (6)$$

where g is the transimpedance gain of the photodetector amplifier (10^5 V/A), R is the detector responsivity (0.58 A/W), NEP is the noise equivalent power of the photodetector (0.8 pW/ $\sqrt{\text{Hz}}$), \hbar is the quantum efficiency of the detector (85%), e is the electronic charge,

P_{ref} is the reference beam power, and E_n is the energy of an 843 nm photon. (Our photodetector is a hybrid photodiode/amplifier from Advanced Photonix, Camarillo, CA, Model SD 100-41-21-231.) The first term in the square root is the amplifier noise, the second is the Poisson term, and the third is the Bose-Einstein photon bunching term.

Measurements of the rms noise in the photodetector output voltage were made as a function of reference beam power and are plotted in Figure 4. The data is described well by

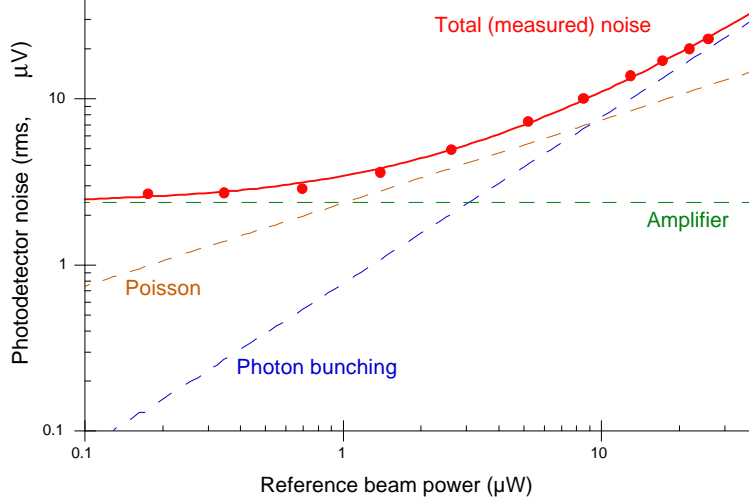


Fig. 4. Photodetector noise as a function of reference beam power. A spectrum analyzer was used to measure the photodetector noise (solid circles) at 122.5 KHz with a bandwidth $BW = 3$ KHz. The theoretical curve (solid line) is calculated using this value of the bandwidth in equation (6).

the theoretical expression in equation (6) with no adjustable parameters. Notice that at the highest reference powers the noise is dominated by photon bunching, and the rms amplitude of the noise is proportional to the reference power.

The output signal of the OCM is the fringe amplitude. Theoretically, when the reference mirror is oscillated with a peak-to-peak displacement amplitude of 0.42λ , and the square root of the sum of powers in equations (2) and (3) is used as a measure of the fringe amplitude, the OCM signal can be expressed as a detector output voltage:

$$V_{rms\ signal} = \frac{1.31 h e g \sqrt{P_{ref} P_{samp}}}{E_n} \quad (7)$$

The OCM signal-to-noise ratio (SNR) is then given by the ratio of equation (7) to equation (6)

$$SNR = \frac{1.31 h e \sqrt{P_{ref} P_{samp}}}{E_n \sqrt{\left[(R \cdot NEP)^2 \cdot BW \right] + \left[2 h e^2 BW \frac{P_{ref}}{E_n} \right] + \left[\left(h e \frac{P_{ref}}{E_n} \right)^2 t_{coh} BW \right]}} \quad (8)$$

When P_{ref} is large, the photon bunching term dominates the noise in the denominator, and the SNR is inversely proportional to the square root of P_{ref} . Hence the SNR decreases with increasing P_{ref} . On the other hand, when P_{ref} is small, the amplifier noise dominates the denominator, and the SNR is proportional to the square root of P_{ref} . The SNR then decreases with decreasing P_{ref} . A peak in the SNR occurs when the photon noise is Poisson distributed.

We looked for this peak in the SNR by focusing the sample beam on the surface of a mirror as neutral density filters were inserted into the reference arm of the interferometer. Figure 5 contains a plot of the measured SNR as a function of P_{ref} . The data is well described by equation (8) except for a multiplicative factor of 0.40. This factor represents a reduction in the heterodyne efficiency due primarily to polarization mixing in the optical fiber of the interferometer. The key result is that we obtain a 40% increase in the SNR by reducing P_{ref} by a factor of 4. Of course, as is evident in equation (8), increasing the power in the sample arm P_{samp} will also increase the SNR.

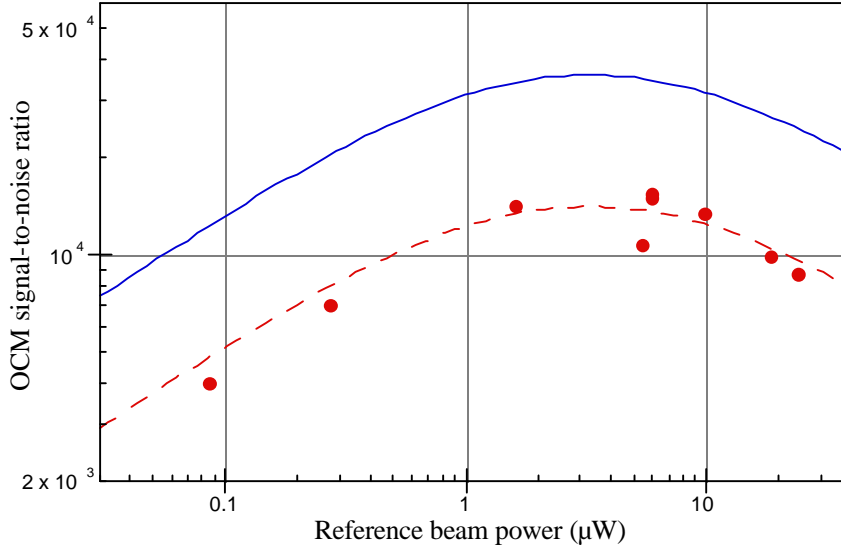


Fig. 5. OCM signal-to-noise ratio as a function of reference beam power. The solid line is calculated from equation (8) with no adjustable parameters. The dashed line includes an additional multiplicative constant of 0.40.

4. Image visualization

Previous researchers [6-10] have rotated and sliced 3-D OCM data sets along selected planes, yielding a series of informative 2-D images. Taken together, these 2-D images can provide insight into the 3-D structure of the sample. We have found, however, that the most effective way to visualize a 3-D data set is to use a technique called volume rendering [19].

In the process of volume rendering, the volume elements (voxels) of the 3-D data set are projected directly onto the 2-D pixels of the viewing screen (computer monitor). For each 2-D pixel, a ray is drawn normal from the viewing screen to and through the sample image. The contents of voxels lying along this ray are “blended” together to yield the contents of the pixel. This procedure can display inner structure such as translucent groups of cells. It is particularly effective when combined with real-time rotation of the viewing direction.

We use the visualization software package Visualization Express (Advanced Visual Systems, Inc., Waltham, MA) to volume-render our 3-D data sets. First we false-color each voxel, assigning red to voxels that back-scatter light strongly, and blue to voxels that back-scatter light weakly. Then the Visualization Express “volume render” module uses the “direct composite” algorithm to blend separately the red, green, and blue contents of voxels into RGB values for pixels. The essential calculation performed by the “direct composite” algorithm is

$$[Pixel_{RGB}] = \sum_n \mathbf{a}_n * [Voxel_{RGB}]_n \quad (9)$$

where $[Pixel_{RGB}]$ is the red, green, or blue value assigned to a particular pixel on the viewing screen, $[Voxel_{RGB}]_n$ are the red, green, or blue contents of voxels lying along the ray generated by the particular pixel, and \mathbf{a}_n are the blending weights (sometimes called “opacity” values) of the voxels. The \mathbf{a}_n are uniquely related to the voxel contents and are typically taken to be proportional to the greyscale voxel contents. The voxel RGB contents, the \mathbf{a}_n , and the pixel values are normalized to lie between 0 and 1. The sum over n in equation (9) begins nearest the viewing screen and proceeds into the sample image. The sum continues until

$$\sum \mathbf{a}_n = 1 \quad (10)$$

Small values of the \mathbf{a}_n mean that many voxels will contribute to a pixel value, and the 2-D image generated will contain information about the interior of the 3-D data set as well as the surface voxels nearest the viewing screen. Larger values for \mathbf{a}_n will yield a 2-D image that is similar to a surface rendering of the data set.

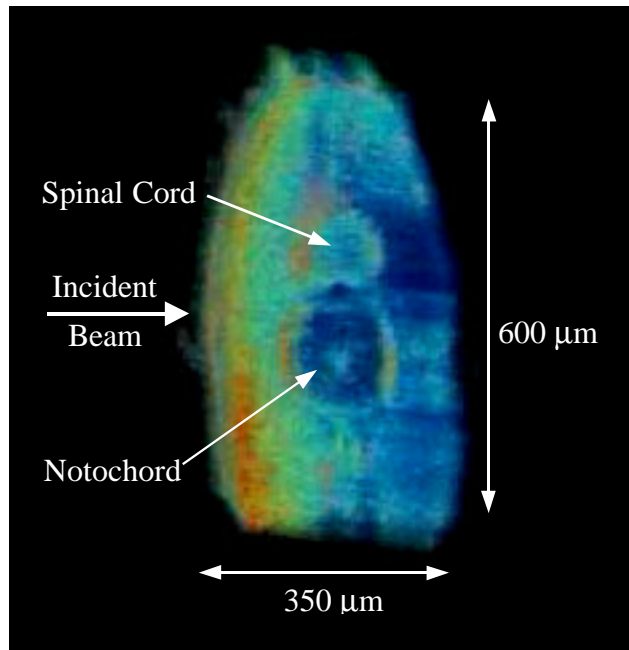


Fig. 6. First frame of the movie of a frog embryo at stage 41 of development. The movie is provided in two sizes: Fig6smal.mov is a 385 kB version with slightly lower resolution than Fig6larg.mov, a 2.46 MB version.

To illustrate these visualization techniques, we include a movie that is a rotating image of a frog embryo (*Xenopus laevis*). The embryo was lightly fixed (2% paraformaldehyde overnight at 4°C) at stage 41 of development (3 days, 4 hours old). Figure 6 contains the first frame of the movie. The view is along the spinal cord, looking from the tail toward the head. The dorsal side (back) is at the top of the figure, and the ventral side (belly) is at the bottom. The beam is incident upon the left side of the embryo. The false color red indicates voxels from which a high intensity of back-scattered light was collected, whereas very little back-scattered light was collected from blue voxels. Notice the general attenuation of light as the beam penetrates the embryo from left to right (red to blue transition in going from left to right in the figure). A typical total attenuation coefficient (scattering plus absorption) is 10/mm for embryos in these later stages of development. Voxels on the far right of the figure receive

incident light that has been attenuated by a factor of roughly $\exp(3.5)$, and the light these voxels back-scatter is further attenuated by $\exp(3.5)$ in traveling back through the embryo.

The spinal cord is a site of high cellular activity at this stage of development, and it scatters light strongly. (Note the shadow to the right of the spinal cord in Figure 6.) On the other hand, the notochord appears dark in Figure 6 because at this stage of development its cells contain large vacuoles. These vacuoles are volumes of water devoid of cellular structures and back-scatter very little light. In general we observe that regions with high cellular activity scatter light strongly, providing a convenient intrinsic probe for critical events in the development of organisms.

Figure 6 is a volume-rendered image of a 3-D region of the embryo that is $600 \mu\text{m} \times 350 \mu\text{m}$ in the plane of the figure and extends $600 \mu\text{m}$ into the figure. The α_n (opacity values) are set low so that the voxels deep in the 3-D image are contributing substantially to the values of pixels in the figure. The 3-D image has been carefully rotated to afford a direct view down the spinal cord and notochord. Rotation of just a few degrees about an axis normal to the spinal cord quickly obscures the structural features that are so obvious at this viewing angle. The movie illustrates this effect as the 3-D image is rotated about a dorsal-ventral axis.

The movie consists of one full rotation (360°) with low opacity values, yielding a translucent, almost diaphanous view of the embryo. These settings accentuate the structure of the spinal cord and notochord. The opacity values are then increased so that surface voxels contribute more to the image, and another full rotation is performed. These settings reveal developing somites that form diagonal stripes (chevrons) in a side-on view. The dark melanophores (pigment cells) are visible in both opacity settings.

We have found that our 3-D OCM images contain useful information about dynamic processes in developing organisms. Our OCM image acquisition time of 5 minutes for a 10^6 voxel image is fast enough to follow events that occur on a time scale slightly longer than the cell division time which can be as short as 10 minutes during embryogenesis. In addition, the proliferation of volume-rendering hardware for use in increasingly fast, inexpensive personal computers bodes well for interactive 3-D visualization of OCM images in the near future.

Acknowledgments

Support for this work has been provided by a Special Opportunity Award from the Whitaker Foundation to Harvey Mudd College and by a National Science Foundation Grant DBI-9612240.